



Cite this: *Green Chem.*, 2021, **23**, 4201

Electrocatalytic hydrogenation of furfural using non-noble-metal electrocatalysts in alkaline medium†

Ram Ji Dixit,^{a,b} Kaustava Bhattacharyya,^{c,b} Vijay K. Ramani ^{*b} and Suddhasatwa Basu ^{*a,d}

The production of bio-oil from agricultural waste is a promising route to improve the agricultural value chain. Herein, furfural (FF), a model bio-oil compound, was subjected to electrocatalytic hydrogenation (ECH) in an alkaline medium to produce economically important furfuryl alcohol (FA) and hydrofuroin (HF). The selectivity of ECH products (FA and HF) on Cu, Pt, and Ni-foam electro-catalysts showed that their generation was dependent upon the availability of H_{ads} , which in turn varied with the choice of electrocatalyst and applied potential. Cu-NP/Ni/NF was obtained through dealloying Cu from a co-electrodeposited Ni-Cu electrode on a Ni-foam substrate, followed by re-electrodeposition of Cu. A porous, high-surface-area bimetallic Ni-Cu catalyst (Cu-NP/Ni/NF) on Ni-foam yielded high rates of FA and HF generation from furfural, e.g. 118.7 ± 8 and 176.3 ± 3.4 $\mu\text{mol h}^{-1} \text{cm}^{-2}$ at -1.45 V vs. Ag/AgCl/sat KCl after 1 h of electrolysis in an alkaline electrolyte. 100% conversion of furfural was observed after 2 h of electrolysis with the same catalyst. The high rate of FA and HF formation was ascribed to enhanced adsorbed FF because of the formation of Cu-nanoplates and bimetallic Ni-Cu. We have provided a rational, high-throughput design for preparing highly active nanoporous electrodes for producing industrially relevant chemicals (furfuryl alcohol and hydrofuroin).

Received 14th February 2021.
Accepted 2nd May 2021

DOI: 10.1039/d1gc00579k

rsc.li/greenchem

1. Introduction

Paddy stubble is lignocellulosic biomass containing 34% cellulose, 23.2% hemicellulose, and 15% lignin, which is 6.7% H, 38.8% C, and 40% O elementally.¹ The paddy stubble that is generated during rice harvesting is usually burnt in China and India due to the unavailability of proper disposal technologies. This stubble has the potential to generate 1500 MW of electricity or \$930 million per year worth of biofuel in a single state (Punjab) alone in India.^{2–4} The U.S. Department of Energy reported in 2016 that approximately one million tons of

biomass are generated across the country that could be used as an alternative source of chemicals and fuels.^{5,6} The thermochemical treatment of agricultural waste, municipal waste, or sewage sludge leads to the production of bio-oil,^{7–9} which can produce fuels and platform chemicals on further processing.¹⁰ Bio-oil is a mixture of organics (~40 wt% O) and water and is acidic in nature. It is a corrosive, chemically unstable, highly viscous, and low vapor pressure liquid that has a low heating value of 19 MJ kg^{-1} , lower than that of diesel or gasoline (44 MJ kg^{-1}).¹¹ The bio-oil can be valorized by subjecting to further chemical treatments (e.g. hydrogenation and hydrodeoxygenation)^{5,12,13} under high temperature (500–600 K) and pressure (5–10 MPa) conditions. Bio-oils contain chemicals that can be polymerized at high temperatures, which can cause plugging and high-pressure drops in the existing petroleum refinery infrastructure during co-processing with crude oil.¹³ The thermal valorization approach has low product selectivity, extreme operating conditions and safety/handling issues, making it economically unattractive. Electrochemical treatment (e.g. electrocatalytic hydrogenation (ECH)) is a promising alternative option for the valorization of bio-oil since it is a low temperature and pressure process that offers *in situ* generation of H_{ads} at the catalyst surface, leading to a greater degree of tuning of products under mild reaction conditions.^{14,15}

^aDepartment of Chemical Engineering, Indian Institute of Technology Delhi, Hauz Khas, New Delhi 110016, India. E-mail: sbasu@iitd.ac.in

^bDepartment of Energy, Environmental & Chemical Engineering, Washington University in St Louis, St Louis 63130, Missouri, USA. E-mail: ramani@wustl.edu

^cChemistry Division, Bhabha Atomic Research Centre, Mumbai 400085, Maharashtra, India

^dCSIR-Institute of Minerals and Materials Technology, Bhubaneswar 751013, India

† Electronic supplementary information (ESI) available: Polarization curves for the HER, cyclic voltammograms, relationship between the current density and scan rate for C_{dl} , R_{FA} and R_{HF} at a working electrode potential of -1.45 V, SEM analysis, % selectivity for all catalysts, XPS survey scan, picture of the Nafion® membrane, change in the FF concentration in the anode compartment with respect to time, and the FF ECH scheme. See DOI: 10.1039/d1gc00579k

Herein, we study furfural (FF) as a bio-oil model compound since it is a relatively abundant constituent (~ 3.5 wt%¹⁶) of crude bio-oil. The ECH of FF generates furfuryl alcohol (FA), hydrofuroin (HF), 2-methyl furan (MF), *n*-butanol, 1,5-pentane-diol, and levulinic acid, which are used in the fuel, pharmaceutical and polymer industries. Our study is mainly focused on FA and HF as both are widely used platform chemicals. FA is used in the foundry industries and in the energy sector^{14,17} while hydrofuroin (market cost $> \$800$ per gram) is a chiral compound that can be used in the production of resins, jet fuels and pharmaceutical molecules such as stereoselective sulfoxide.^{18,19} The separation of FF, FA, and HF can be achieved through distillation or liquid-liquid extraction.²⁰

The product selectivity (*S*) and faradaic efficiency (FE) in ECH reactions depend upon the nature of the catalyst, applied potential, electrolyte pH, initial concentration of reactants, and temperature. To date, ECH of FF has been reported on various electrocatalysts such as Cu, Ni, Pb, Fe, and Pt, over the entire pH range. The *S* and FE of products generated by FF ECH are correlated with the hydrogen evolution reaction (HER) overpotential, generating FA on low HER overpotential metals (Pt and Ni) and pinacol derivatives on high HER overpotential metals (Pb, Fe, and Al).²¹ Under mild basic conditions (carbonate buffer), the trend in HER overpotential is as follows: Pt < Ni < Cu < Pb; Cu is the most active element for ECH.²² The carbon free radical generated by the direct transfer of an electron to the CHO moiety of FF is responsible for the higher Y_{FA} and FE_{FA} on the Cu catalyst. Li's group²³ provided broad insights into the mechanism of FF reduction in 0.5 M sulfate solution (pH = 3) or 0.5 M sulfuric acid (pH = 0.5) using electrodes modified with organothiol self-assembled monolayers to control the diffusion of the reactants on the surface. They concluded that inner sphere and outer sphere electron transfer reactions occurred for FA and HF generation, respectively. FA (pH = 3, S_{FA} = 39.6%; pH = 0.5, S_{FA} = 11%) and MF (pH = 3, S_{MF} = 15.4%; pH = 0.5, S_{MF} = 66.8%) were produced by the direct interaction of FF with the Cu electrode, while HF formation did not require the direct interaction with the Cu electrode (pH = 3, S_{HF} = 6.2%; pH = 0.5, S_{HF} = 1.8%). Zhao *et al.*²⁴ reported 3 wt% Pt/ACF as an active catalyst for the ECH of FF at pH = 1 (S_{FA} = 99%, FE_{FA} = 78%). An increase in temperature up to 50 °C enhanced FE_{FA} up to 85% but a further increase in temperature decreased FE_{FA} . La-Doped TiO₂ increased the current density during the ECH of FF in DMF due to the formation of the redox couple TiO₂/Ti(OH)₃ and lattice distortion (S_{FA} = 88.6%).²⁵ The addition of an organic co-solvent also influenced the yield as an electrolyte of 50% acetonitrile (v/v, pH = 0) showed a high yield on a Cu-electrode (S_{FA} = 36.4%).²⁶ It was also observed that low pH (~ 0) and moderate pH ($\sim 3-4$) promoted high efficiencies for MF and FA formation, respectively.^{23,26} HF production on Pb and Cd was analyzed in 10% KH₂PO₄ electrolyte at 10 mA cm⁻² current density and HF yields were 48% and 43%, respectively.²⁰ Sun's group¹⁹ reported HF formation using carbon paper as an electrode in batch and continuous modes using FF in 0.5 M H₂SO₄ (pH = 0), 0.1 M KPi (pH = 7), and 0.1 M KOH (pH = 13) and obtained

a high HF yield ($\sim 94\%$) and FE_{HF} ($\sim 93\%$) in 0.1 M KOH. Though most of the reports show FF-treatment in acidic or buffered media, handling problems arise due to the polymerization of FF under acidic conditions.²⁷ One solution is to perform ECH in an alkaline medium since this (i) enhances the conductivity of bio-oil (pH = 9, conductivity = 21 mS cm⁻¹)²⁸ and thereby reduces the solution resistance for ECH, (ii) lowers the bio-oil polymerization rate, thereby enhancing handling capability, and (iii) expands the material space of electrocatalysts since non-noble transition metal based electrocatalysts are unstable in acidic medium but can be effective in alkaline medium.^{29,30} FF also undergoes the Cannizzaro reaction³¹ in alkaline medium to form FA and furoic acid, and the FF conversion rate is high under highly alkaline conditions. We chose 0.5 M NaOH as the supporting electrolyte for ECH so that FA and furoic acid formation through the Cannizzaro reaction was minimized.

The morphology of the catalyst and electrode plays an important role during ECH. An electrode having high active site density and surface area, good mechanical stability, and properly tuned active site coordination numbers typically will exhibit higher activity.^{33,34} Mass transfer limitations within the electrode pore-structure are a critical factor governing the overall rate and selectivity of ECH, making pore size tuning and optimization necessary.³⁵

In this work, the ECH of FF was investigated on Cu, Ni-Foam (NF), and Pt in alkaline medium to analyze their activity towards FA and HF production. A binder-free porous Ni structure was developed *in situ* on a NF substrate by a facile electrochemical method. Cyclic voltammetry was performed to obtain the reduction and oxidation potentials of Ni and Cu ions, and these potentials were further employed for subsequent co-deposition and etching. The porosity and inter-pore spacing were optimized to obtain high HER currents. Cu was electrodeposited on optimized porous Ni to get bimetallic Ni-Cu. The rate of formation and selectivity towards FA and HF were then obtained on the optimized catalysts at various potentials and time intervals. The products were detected by gas chromatography-mass spectrometry and quantified by high-performance liquid chromatography. The FF ECH mechanism was advanced for all three optimized electrodes, NF, porous Ni, and bimetallic Ni-Cu, before and after electrolysis, to determine the change in the electronic environment and to guide selectivity tuning.

2. Experimental

2.1 Catalyst preparation

Cu and Pt plates were pretreated using the following steps before use: polishing by 600 grit sandpaper, immersing in 1 M HCl for 1 h followed by rinsing with DI water and drying. NF was used as the conductive substrate for all the electrodes prepared by the electrochemical method due to its high surface area and 3D hierarchical pore structure.³⁶ NF was pretreated by ultra-sonication in acetone for 10 min for degreasing, followed by rinsing with DI water and drying. Nano-porous Ni

supported on NF was prepared by the template-free selective electrochemical etching of Cu from co-deposited Ni–Cu.³⁷ The electrochemical co-deposition was performed in a standard three-electrode undivided electrochemical system of volume 300 mL. NF (10 cm²), Pt plate, and Ag/AgCl/sat KCl (Pine Research) were used as working, counter, and reference electrodes, respectively, for all the electrodeposition processes. All the electrode potentials were reported against Ag/AgCl/sat KCl. The Pt plate was polished by 600 grit sandpaper followed by rinsing with DI water before every experiment. The deposition potentials of Ni²⁺ and Cu²⁺ were obtained using cyclic voltammetry (CV) with Ni(II) (0.6 M NiSO₄·6H₂O with 0.5 M H₃BO₃), Cu(II) (0.02 M CuSO₄·5H₂O with 0.5 M H₃BO₃), and Ni(II) + Cu(II) (0.6 M NiSO₄·6H₂O, 0.02 M CuSO₄·5H₂O with 0.5 M H₃BO₃) electrolytes. The scan rate and potential range for CV were 50 mV s⁻¹ and 0.8 V to -1.2 V respectively. The co-deposited Ni–Cu on NF was prepared by using 0.6 M NiSO₄·6H₂O, *x* M (0.01 < *x* < 0.04) CuSO₄·5H₂O, and 0.5 M H₃BO₃ (pH = 4) as electrolytes at -0.85 V with the deposition duration of *y* minutes (10 < *y* < 40). Subsequently, a potential of 0.5 V was applied to the resulting Ni–Cu-deposited NF electrodes to etch out Cu selectively to yield a porous Ni array on the NF. The samples were designated as *x*-*y*-NPNi/NF. The values of *x* and *y* were optimized to get the best HER current in 0.5 M NaOH electrolyte. Cu was subsequently electrochemically deposited on optimized *x*-*y*-NPNi/NF using 0.02 M CuSO₄·5H₂O and 0.5 M H₃BO₃ as electrolytes at -0.85 V for *z* minutes (5 < *z* < 30) of electrodeposition. This catalyst was designated as 0.02 *z* Cu-0.02 40 NPNi/NF and the value of *z* was optimized on the basis of the rate of formation of FA. The specific catalysts (including benchmarks) prepared and evaluated are tabulated in Table S1.†

2.2 Electrochemical analysis

All electrochemical analyses were performed using a Gamry Instruments Version 5.6, 2009 electrochemical workstation equipped with Gamry Echem Analyst software. Linear sweep voltammetry (LSV), cyclic voltammetry (CV), and chronoamperometry were used to analyze the electrochemical behavior of the electrocatalysts. Electrochemical analyses were performed in a H-type electrochemical cell with distinct anode and cathode compartments (200 mL each), separated by a Nafion® 117 membrane. The compartments were filled with 150 mL of electrolyte. The reference electrode and counter electrode used were Ag/AgCl/sat KCl, and Pt plate, respectively. The prepared electrodes described earlier (Table S1†) were used as the working electrodes. All the obtained currents were reported in the form of current density (mA cm⁻²) by normalizing them with the projected geometrical surface area (10 cm²) accounting for both sides of the working electrode. 50 mM FF in 0.5 M NaOH was used as the electrolyte for studying the ECH. The NaOH electrolyte was purged with N₂ starting 15 min prior to FF addition, and continued till the end of each analysis. Unless otherwise mentioned, all the LSVs were recorded in the potential range of 0 to -1.13 V at a scan rate of 50 mV s⁻¹. The electrochemical double layer capacitance (*C*_{dl}) was analyzed by performing CV experiments at various scan

rates (20, 50, 100, and 200 mV s⁻¹) in 0.5 M NaOH electrolyte over the potential range of -0.1 V to -0.5 V. The difference between the anodic and cathodic currents, Δ*J*_{-0.3 V} (*J*_a - *J*_c at -0.3 V), was plotted against the scan rate and the slope of the curve was related to the *C*_{dl} (slope = 2*C*_{dl}).³⁸ The electrochemically active surface area (ECSA) was calculated on the basis of the obtained *C*_{dl}. All the potentials were *iR* corrected to compensate for the potential drop due to internal resistance. Electrolysis was initially performed in the potentiostatic mode for 1 h to optimize the potential range for FA generation, followed by an increase in the electrolysis duration up to 3 h to obtain 100% conversion of FF. All the experiments were performed at ambient temperature and pressure.

2.3 Product analysis

FA and HF were generated by FF ECH and FA was also generated by the Cannizzaro reaction.³¹ Samples collected from the product mixture were analyzed by a gas chromatograph-mass spectrometer (GC-MS) (Agilent 7890 A) equipped with a HP-5MS capillary column (30 m × 0.25 mm, 0.25 μm) and an FID detector. Extraction of the organic phase was performed by mixing the collected samples with diethyl ether (1 : 1 v/v) followed by vigorous stirring (1 h) and leaving the mixture overnight to equilibrate. Subsequently, the organic phase was collected, filtered with a 0.22 μm filter and injected into the GC-MS. The injector was set at 250 °C and 1 μL of injection was made in the 10 : 1 split mode. N₂ was used as the carrier gas at a flow rate of 1 mL min⁻¹. The MS ion source and quad temperatures were 230 °C and 150 °C, respectively. The GC-MS program was started by maintaining the oven at 40 °C, halted for 3 min, followed by heating up to 280 °C with a heating rate of 10 °C min⁻¹.³⁹ Identification of products was primarily done by comparing the mass spectra against the National Institute of Standards and Technology (NIST) mass spectral library. Thereafter, the standards were run through the GC-MS to reinforce product confirmation.

For NMR analysis, the electrolyte was mixed with ether (1 : 1 v/v) and stirred for 3 h, leaving the mixture for attaining equilibrium for 12 h. The aqueous and organic phases were separated from which the organic phase was collected. The ether present in the organic phase was completely evaporated, and the remaining organics were mixed with 0.5 mL of D₂O. ¹H and ¹³C-NMR spectra were obtained using a Bruker Ascend™ 400 MHz NMR. The presence of FA and HF was confirmed by the NMR spectra (Fig. S11†).^{19,40}

The quantification of chemicals was performed by high-performance liquid chromatography (HPLC) (Agilent 1100) equipped with an Agilent C₁₈ column (Zorbax 300 SB-C18; 4.6 mm × 150 mm, 3.5 μm) and a diode-array detector. The samples were collected from the product mixture, diluted by mixing with DI water (1 : 1 v/v) and filtered with a 0.22 μm filter. 1 μL of the sample was injected under the following conditions: column temperature = 22 °C, mobile phase = acetonitrile (10% v/v) with water (90% v/v), and flow rate = 1 mL min⁻¹. The wavelengths were chosen to be 215 nm and 253 nm because of the variable product mixture. The rate of

formation, selectivity, and conversion were calculated using the below equations for all the products.

The moles of products or reactants in this study were corrected to eliminate the contribution of non-electrochemical reactions (*e.g.*, Cannizzaro reaction) to ensure only the conversion due to ECH was considered. The moles of organic compounds formed or consumed due to electrolysis (n^E) were calculated as follows:

$$n^E = n^{E+B} - n^B$$

where, n^{E+B} is the moles obtained by taking the sample from the reactor at time t with the potential applied at $t = 0$, which comprises all electrochemical, chemical and physical processes, whereas n^B (Blank run) corresponds to the samples taken at identical time t , wherein no electrochemical potential was applied to the system, thereby comprising the non-electrochemical processes.

1. R_P was the rate of formation of product P (FA or HF) in $\mu\text{mol h}^{-1} \text{cm}^{-2}$ and was calculated using the following equation.

$$R_P = \frac{C_P^E \times V}{t \times A};$$

where C_P^E is the concentration of the product (P is FA or HF) generated due to electrolysis, V is the catholyte volume (150 mL), R_P

was calculated after 1 h of ECH for all the catalysts, and A is the geometric area of the electrode (10 cm^2).

$$\% \text{Selectivity}(\%S_P)^{41} =$$

$$2. \frac{\text{moles of FF converted to form product P due to ECH} \times 100}{\text{moles of FF converted due to ECH}}$$

$$\% \text{Conversion of FF due to ECH}(\%C)^{41} =$$

$$3. \frac{\text{moles of FF converted due to ECH} \times 100}{\text{initial moles of FF}}$$

$$\text{Carbon recovery}(\%) =$$

$$4. \frac{(\text{weight of carbon at } t = 0 - \text{weight of carbon at } t)}{\text{weight of carbon at } t = 0} \times 100.$$

3. Results and discussion

3.1 Preparation and optimization of electrocatalysts

The NF was modified to develop a nanoporous Ni electrode using electrochemical co-deposition of Ni and Cu followed by selective electrochemical etching of Cu. To determine the potentials for deposition and etching, CV experiments were performed using Ni(II), Cu(II) and Ni(II) + Cu(II) electrolytes (Fig. 1). In the case of the Ni(II) electrolyte, a reduction peak at -0.54 V indicated the deposition of Ni ($E_{\text{Ni}^{2+}/\text{Ni}^0} = -0.45 \text{ V}$) (Fig. 1a).⁴² Two oxidation peaks at 0.06 V and 0.21 V during the anodic scan (forward scan) are attributed to the dis-

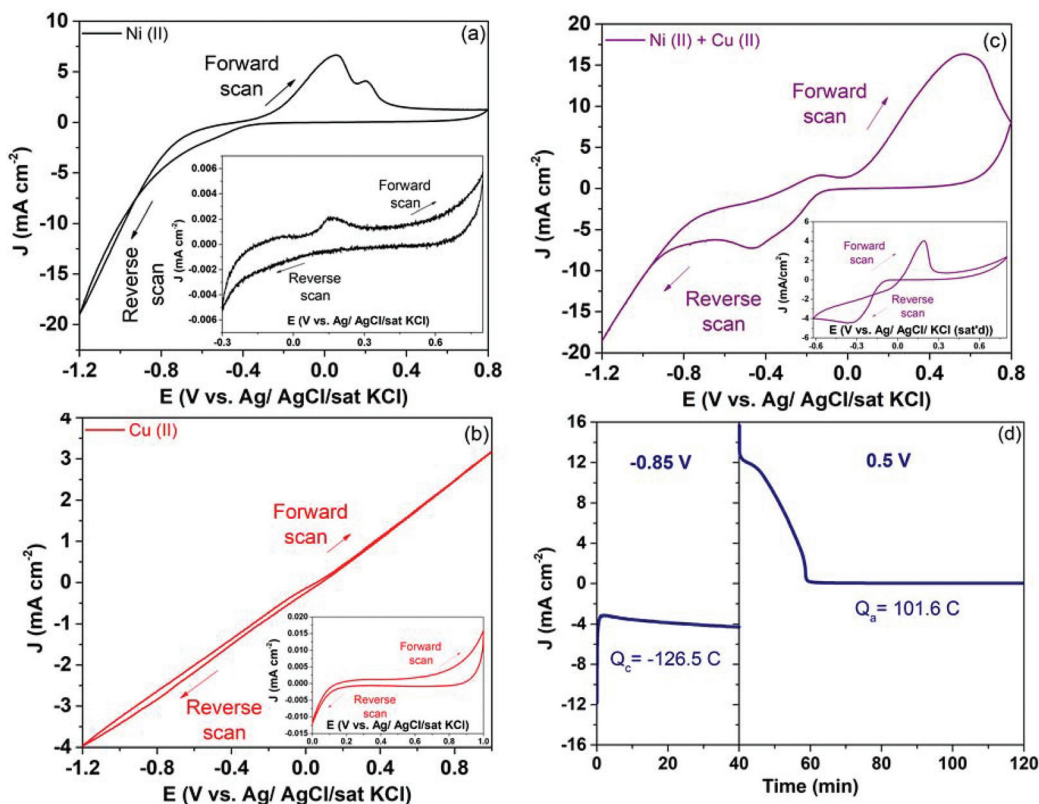


Fig. 1 Cyclic voltammetry for the reduction and oxidation of (a) Ni using 0.6 M NiSO₄·6H₂O with 0.5 M H₃BO₃ (Ni(II)), (b) Cu using 0.02 M CuSO₄·5H₂O with 0.5 M H₃BO₃ (Cu(II)), (c) Ni–Cu using 0.6 M NiSO₄·6H₂O, 0.02 M CuSO₄·5H₂O with 0.5 M H₃BO₃ (Ni(II) + Cu(II)). Inset figures are respective experiments with a small potential window. (d) Chronoamperometry using the Ni(II) + Cu(II) electrolyte for 40 min at -0.85 V followed by 80 min at 0.5 V . Q_c is the charge involved during reduction and Q_a is the charge involved during oxidation. Substrate: Ni-foam, scan rate: 50 mV s^{-1} .

solution/passivation of α -Ni and β -Ni, respectively.⁴³ In the case of the Cu(II) electrolyte, the deposition of Cu started at ~ 0.08 V ($E_{\text{Cu}^{2+}/\text{Cu}^0} = 0.143$ V) (Fig. 1b). In the Ni(II) + Cu(II) electrolyte, similar reduction currents and peaks at a potential of 0.0 V and -0.46 V are attributed to Cu^{2+} and Ni^{2+} reduction, respectively (Fig. 1c). During the anodic scan (forward scan), a broad oxidation peak at 0.58 V was attributed to the combined effect of passivation/dissolution of Ni and Cu (Fig. 1c). The Ni–Cu co-deposition and oxidation potentials were selected as -0.85 V and 0.5 V, respectively, from the above CV analyses. Chronoamperometry was performed using the Ni(II) + Cu(II) electrolyte at -0.85 V and 0.5 V with the reaction duration of 40 min and 80 min, respectively, to obtain nanoporous Ni. The chronoamperometric analysis indicated the continuous deposition of Ni^{2+} and Cu^{2+} during reduction followed by metal etching during oxidation (Fig. 1d). The selective etching of Cu during oxidation was confirmed by energy-dispersive X-ray spectroscopy (EDXS) (Fig. S4d, e and g[†]), which yielded a porous Ni electrode. The increase in the oxygen content during oxidation confirmed the passivation of the Ni-surface (Fig. S4g[†]).

The surface roughness and pore-size of the electrode were tuned by modulating the Cu concentration in the electrolyte solution and the co-electrodeposition time (Table S1 and Fig. S1[†]). The HER was performed to show the extent of hydrogen coverage on the roughened surface and its pores under cathodic conditions (0 to -1.13 V) suggesting 0.02–40-NPNi/NF (designated as NPNi/NF), which resulted in the best HER activity. A 10-fold increase in the ECSA for NPNi/NF was observed in comparison with the pristine NF electrode (Fig. S2[†]), illustrating high surface roughness for the syn-

thesized electrodes. Subsequently, Cu was electrochemically deposited onto the NPNi/NF surface to increase the activity for the FF ECH, which was the highest for Cu–NPNi/NF (Table S1 and Fig. S3[†]). This sample was used for further ECH studies.

Inspection of the SEM images revealed that optimized NPNi/NF had a rough morphology (Fig. 2a, b, and S4b[†]). The large pore size range (200–260 nm) and inter-pore spacing for NPNi/NF facilitated the effective diffusion of reactants and products, confirmed *via* HER current density enhancement (Fig. S1[†]).³⁶ Upon electrodepositing Cu on NPNi/NF (Cu–NPNi/NF), SEM images depicted the formation of Cu nanoplates (Fig. 2c). The XRD of Cu–NPNi/NF shows the characteristic diffraction features of Ni and Cu metals. The XRD features could be indexed to the (111), (200), and (220) planes of face-centered cubic Ni (JCPDS: 87-0712) and face-centered cubic Cu (JCPDS: 89-2838) as shown in Fig. 2d. The formation of Cu–Ni alloy requires the appearance of distinct features apart from pure Cu and Ni metals,⁴⁴ which was not observed for Cu–NPNi/NF. However, a slight positive shift in the XRD features of Cu planes indicated a small interaction of Cu and Ni planes suggesting the formation of bimetallic Cu–Ni,⁴⁵ which is also observed by XPS (Fig. S10[†]). Elemental mapping by EDXS (Fig. 2f) showed preferential Cu deposition on pore vertices as compared to pore bases of the NPNi/NF substrate due to diffusion limitations of the Cu ion.⁴⁶ The XPS survey scan showed the presence of Ni and O in NF, and the presence of Ni, Cu and O in NPNi/NF and Cu–NPNi/NF (Fig. S7a and b[†]). The trend in at% obtained from both XPS and EDXS analyses confirmed the presence of Cu along with Ni in the Cu–NPNi/NF catalyst (Table 1). As the reactions occur only on the surface, XPS measurements were chosen for further analyses.

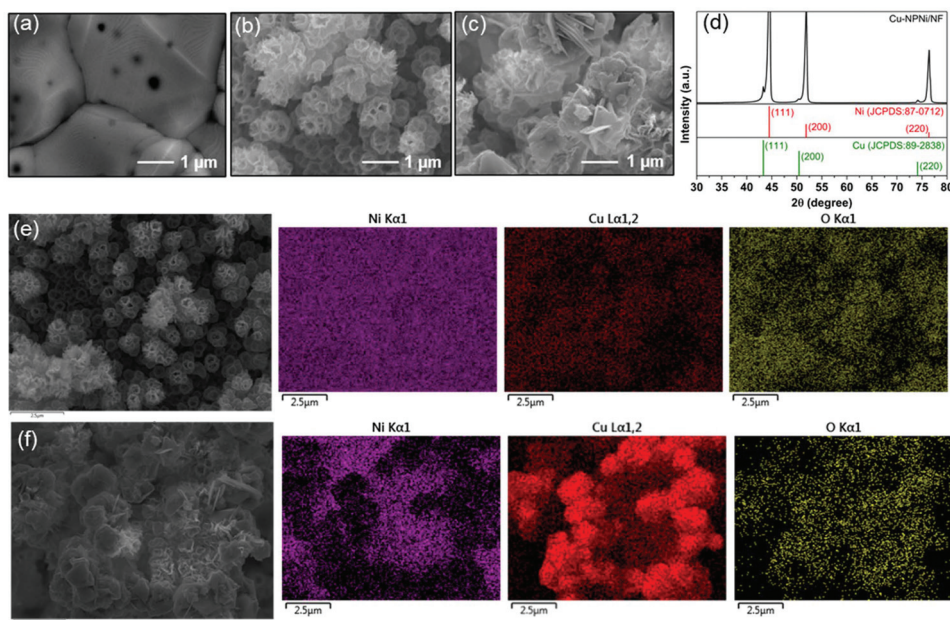


Fig. 2 SEM images for (a) pristine Ni-foam (NF), (b) NPNi/NF, (c) Cu–NPNi/NF. (d) XRD of Cu–NPNi/NF. Elemental mapping of (e) NPNi/NF and (f) Cu–NPNi/NF.

Table 1 Elemental concentration of Ni, Cu, and O obtained by EDXS and XPS for NF, NPNI/NF, and Cu–NPNI/NF before and after FF ECH

Sl no.	Type of sample	Elemental concentration from EDXS (at%)			Elemental concentration from XPS (at%)		
		Ni	Cu	O	Ni	Cu	O
1	NF	98.7	0	1.3	36.75	—	63.25
2	NPNI/NF	84.4	1.8	13.8	32.11	1.20	66.69
3	Cu–NPNI/NF	15.6	77.0	7.4	16.96	8.18	74.86
4	NF, FF	—	—	—	18.02	—	81.98
5	NPNI/NF, FF	—	—	—	4.41	1.15	94.44
6	Cu–NPNI/NF, FF	—	—	—	0.87	1.15	97.98

3.2 Electrocatalytic hydrogenation of furfural in an alkaline electrolyte

Chronoamperometry analysis was performed to analyze FF ECH by studying 0.5 M NaOH with and without FF (the latter being the blank experiment). A potential of -1.45 V was applied for 1 h on the following working electrodes: NF, NPNI/NF and Cu–NPNI/NF. In each case, the reduction current approached more positive values with time due to the decrease in FF concentration owing to ECH; no change in reduction current was observed in the blank experiment (Fig. S5c†). The

ECH of FF yielded FA and HF in an alkaline electrolyte. The formation rate and selectivity of FA (R_{FA} , % S_{FA}) and HF (R_{HF} , % S_{HF}) on NPNI/NF and Cu–NPNI/NF were benchmarked against Cu, Pt, and NF by performing chronoamperometry at various applied working electrode potentials (Fig. 3a, b and Table S3†). Upon analyzing the R_{FA} and R_{HF} for benchmark Cu, Pt and NF, we observed that FA formation started at an applied working electrode potential of -1.15 V for all the three catalysts while HF formation started at -1.15 V for Cu and -1.25 for Pt and NF. The binding energy of FF was calculated using density functional theory and reported to be -1.86 eV,⁴⁷

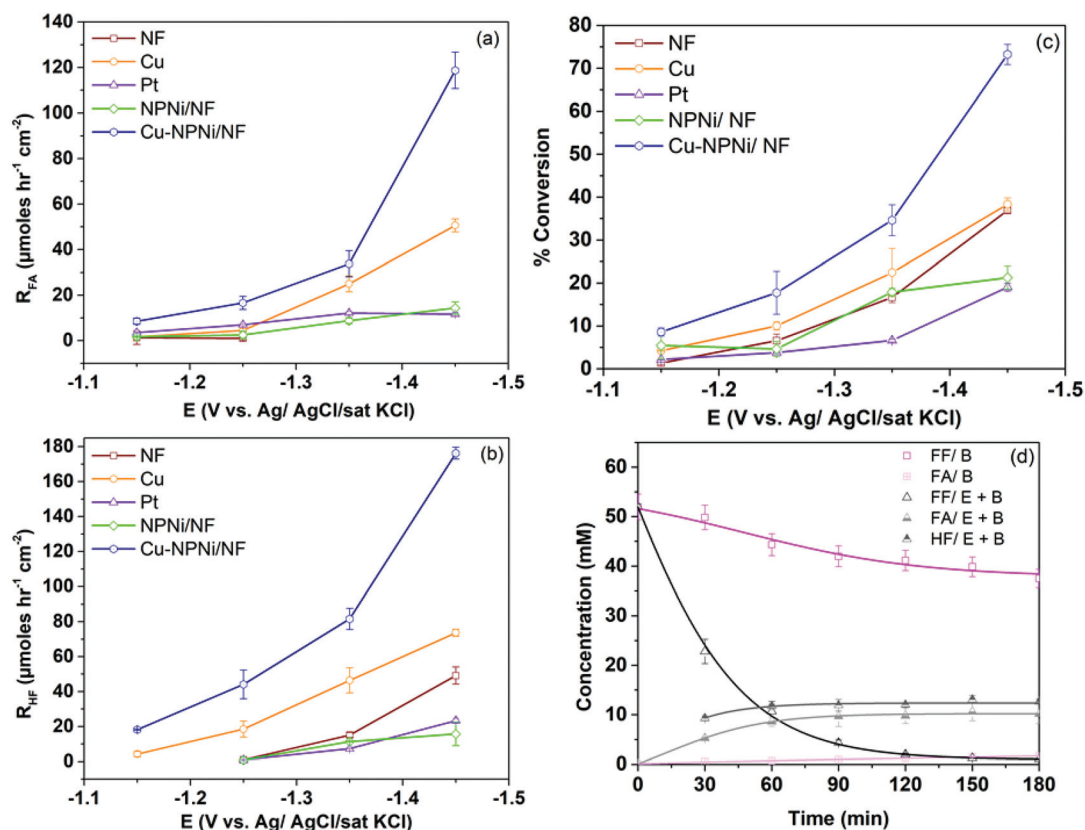


Fig. 3 (a) Rate of formation of FA (R_{FA}), (b) rate of formation of HF (R_{HF}), (c) % conversion of FF at potentials: -1.15 V; -1.25 V; -1.35 V; -1.45 V, working electrodes: NF, Cu, Pt, NPNI/NF, and Cu–NPNI/NF, electrolyte: 0.5 M NaOH + 50 mM FF, and electrolysis duration: 1 h. (d) Change in concentration of FF, FA and HF with respect to time for blank (B, without potential) and with electrolysis (E + B) at -1.45 V using Cu–NPNI/NF. 0.5 M NaOH + 50 mM FF was used as the electrolyte for all the reaction conditions.

-1.59 eV,⁴⁸ and -0.66 eV (ref. 48), respectively, for Pt (111), Ni (111), and Cu (111). This indicated stronger adsorption of FF on the surface for Pt and Ni as compared to Cu. Since FF was bound more strongly on Pt and NF, the FF ECH reaction occurred at a higher potential for these catalysts relative to Cu. The C–H coupling required for FA generation did not require significant additional overpotential, and hence FA was generated at -1.15 V on all catalysts. Cu also facilitated the specific adsorption of $-O$ from the $-CHO$ moiety of FF such that the aromatic furan ring of FF was positioned away from the catalyst surface, in contrast to Pt and Ni wherein aromatic furan ring adsorption was favored.^{47,48} The adsorbed complexes on the surface of Pt and NF were less facile as compared to Cu, which limited the R_{FA} and R_{HF} for the former as compared to the latter.^{48,49} Comparing the rate of formation of FA and HF based on the geometric area and ECSA indicated that Cu had higher intrinsic activity for FF ECH than Pt and NF (Table S2†).

% S_{FA} and % S_{HF} were noted for the Pt electrocatalyst at -1.25 V and -1.45 V (Table S3†) and showed a decrease in FA selectivity and an increase in HF selectivity at higher potentials. Pt is known to generate H_2 from H_{ads} at very high rates at high potentials. This favored faster H_{ads} depletion to H_2 compared to the rate of transfer of H_2O at the electrode surface. Hence, the limited availability of H_{ads} at higher potentials favored HF formation.²³ The availability of FF_{ads} and H_{ads} required for FA production (Scheme S1 in ESI†). FA could be diminished if any of these species (FF_{ads} and H_{ads}) became limited on the surface. FF conversion (Fig. 3c) for all the electrocatalysts showed that FF transport to the electrode surface was not the limiting factor. H_{ads} generation was more facile on Pt as compared to NF and this led to more R_{FA} , % S_{FA} on Pt. Similar results were obtained by Sun's group using carbon paper and Cu electrodes suggesting that HF was formed on carbon paper due to the low H_{ads} concentration, however, HF and FA were formed at Cu due to an enhanced H_{ads} .¹⁹ H_{ads} can also be increased by changing the morphology and electronic structure of the catalyst surface;⁵⁰ therefore, NF was modified to obtain NPNi/NF. NPNi/NF exhibited an enhanced surface area and functionality, which resulted in an enhanced HER (H_{ads}) (Fig. S1†). The increase in R_{FA} , % S_{FA} and decrease in R_{HF} , % S_{HF} observed for NPNi/NF as compared to NF was due to the elevated H_{ads} seen in NPNi/NF (Fig. 3, Tables S2 and S3†). The comparison of NF with Pt and NPNi/NF confirmed the role of H_{ads} in obtaining more selectivity for FA.

Cu was used as a benchmark due to its high intrinsic activity for FF conversion in an alkaline medium. The high surface area micro-crystalline structure of Cu provided higher FF conversion than bare Cu foil.⁵¹ Cu–NPNi/NF was prepared by the electro-deposition of Cu nanoplates on the NPNi/NF (Fig. 2c). Cu is known for its FF_{ads} property⁵¹ and the formation of nanoplates provided enhanced surface-active sites, which contributed to enhanced FF_{ads} . The formation of bimetallic Ni–Cu using electrochemical deposition has been reported⁵² and bimetallic formation was also confirmed for the synthesized Cu–NPNi/NF using XPS analysis. The Ni and

Cu content in the Cu–NPNi/NF was 16.96 and 8.18 at% respectively (Table 1). The alloying of a smaller concentration of Cu in the Ni bulk decreased the gap between the fermi-energy level and d-band,⁵³ which facilitated enhanced chemisorption of species (FF_{ads} and H_{ads} in our study) on the catalyst surface. For Cu–NPNi/NF, the rate of formation of FA and HF based on the ECSA was $3.2 \mu\text{mol h}^{-1} \text{cm}_{ECSA}^{-2}$ and $4.7 \mu\text{mol h}^{-1} \text{cm}_{ECSA}^{-2}$, respectively, which were higher than that of NPNi/NF indicating both active sites increase and bimetallic Cu–Ni formation facilitates FF ECH (Table S2†). The R_{FA} ($118.7 \pm 8 \mu\text{mol h}^{-1} \text{cm}^{-2}$), R_{HF} ($176.3 \pm 3.4 \mu\text{mol h}^{-1} \text{cm}^{-2}$), % S_{FA} ($21.6 \pm 1.1\%$), and % S_{HF} ($64.2 \pm 3.2\%$) were higher for Cu–NPNi/NF as compared to Cu, NF and NPNi/NF. The performances reported in previous studies were re-formulated for consistency based on our standard definitions (Section 2.5) and are reported in Table 2. To the best of our knowledge, the Cu–NPNi/NF catalyst studied herein showed the highest R_{FA} and R_{HF} in an alkaline electrolyte based on all reports to date using non-noble metal catalysts (Table 2). The ECH of hydroxymethylfurfural was performed in previous literature studies using Ag considering it a benchmark catalyst to obtain a significant ECH performance,^{54,55} however, FF ECH has not been reported to date using Ag. We electrodeposited Ag on NF (ed-Ag/NF) and characterized it as mentioned in the ESI.† FF ECH using ed-Ag/NF was compared with the Cu–NPNi/NF under the same operating conditions (applied potential, electrolysis duration, and electrolyte) to provide a precise comparison (Table 2). The R_{FA} , % S_{FA} were lower and R_{HF} , % S_{HF} were higher for Cu–NPNi/NF than those of ed-Ag/NF indicating comparable FF ECH performances while considering both FA and HF as the products of interest.

The ECH and electroreduction (ER) mechanisms were obtained for the formation of FA and HF, respectively, in an acidic supporting electrolyte, which is unclear in an alkaline supporting electrolyte.^{23,55} ECH involves the direct interaction of reactant species (FF and H_2O) with the electrode surface for FF conversion, whereas ER occurs in the electrolyte without a specific reactant and surface interaction. To obtain mechanistic insights into FA and HF generation at the Cu–NPNi/NF electrocatalyst in the alkaline supporting electrolyte, we performed experiments with distinct initial FF concentrations (10 mM, 50 mM, and 100 mM). The R_{FA} was increased and % S_{FA} was decreased along with an increase in R_{HF} and % S_{HF} at high initial FF concentrations (Table 2). An increase in the FF concentration limited the H_{ads} concentration at the surface resulting in the decrease of % S_{FA} . An increase in the FF_{ads} concentration increased R_{FA} and R_{HF} . Therefore, FA formation was dependent upon the FF_{ads} and H_{ads} concentrations following the ECH mechanism,⁵⁵ whereas R_{HF} and % S_{HF} could be increased either due to the ECH or ER. Nafion® (5 wt%) was coated on the surface of Cu–NPNi/NF to restrict the direct FF interaction with the surface. The R_{FA} and R_{HF} were decreased for Nafion®/Cu–NPNi/NF samples compared to Cu–NPNi/NF samples due to the decrease in the FF_{ads} concentration (Table 2 and Table S4†) indicating the requirement of strong interaction of FF and H_2O with the electrocatalyst surface.²³

Table 2 Comparison of FF conversion along with the rate of formation (*R*), and selectivity (*S*) for FA and HF with previously reported literature studies

Cathode	Electrolyte	Potential/current density and electrolysis duration	Furfuryl alcohol	Hydrofuroin	% Furfural conversion	Ref.
Cu-NPNI/NF	0.5 M NaOH 10 mM FF	-0.45 V vs. RHE ^a (-1.45 V vs. Ag/AgCl/sat KCl) 1 h	$R_{FA} = 83.9 \pm 2.1^c$ $S_{FA} = 74.3 \pm 3.0^d$	$R_{HF} = 8.9 \pm 0.67$ $S_{HF} = 15.8 \pm 0.9$	75.2 ± 4.0%	Our work
Cu-NPNI/NF	0.5 M NaOH 50 mM FF	-0.45 V vs. RHE ^a 1 h	$R_{FA} = 118.7 \pm 8^c$ $S_{FA} = 21.6 \pm 1.1^d$	$R_{HF} = 176.3 \pm 3.4$ $S_{HF} = 64.2 \pm 3.2$	73.2 ± 2.3%	Our work
Cu-NPNI/NF	0.5 M NaOH 100 mM FF	-0.45 V vs. RHE ^a 1 h	$R_{FA} = 135.0 \pm 5.6^c$ $S_{FA} = 13.6 \pm 0.6^d$	$R_{HF} = 341.1 \pm 11.2$ $S_{HF} = 68.7 \pm 3.2$	66.2 ± 2.8	Our work
ed-Ag/NF	0.5 M NaOH 50 mM FF	-0.45 V vs. RHE ^a 1 h	$R_{FA} = 156.7 \pm 9.4^c$ $S_{FA} = 29.6 \pm 1.8^d$	$R_{HF} = 125.0 \pm 5.8$ $S_{HF} = 47.2 \pm 3.2$	70.6 ± 3.5	Our work
Carbon paper	0.1 M KOH 10 mM FF	2.1 V ^b	NA	$R_{HF} = 130^e$	NA	19
Cu ₃ P/CFC	1 M KOH 50 mM FF	1.4 V ^b 10 mA cm ⁻² ^b 1 h	$R_{FA} = 90.75^c$ $S_{FA} = \sim 100^d$	NA	37.5%	66
Cu/Cu foil-400 nm	0.5 M H ₂ SO ₄ with H ₂ O/CH ₃ CN (4/1 v/v) 100 mM FF	-0.80 V vs. RHE 1 h	$R_{FA} = 60.0^c$ $S_{FA} = 15.79^d$	NA	76.0%	51
Cu foil	0.5 M Sulphate solution (pH = 3) with CH ₃ CN (25% v/v) 50 mM FF	-0.55 V vs. RHE 1 h	$R_{FA} = 12.99^c$ $S_{FA} = 39.6^d$	$R_{HF} = 1.02$ $S_{HF} = 6.2$	16.4%	23

^a $E_{RHE} = E_{Ag/AgCl}^{\circ} + 0.059 \times \text{pH} + E_{Ag/AgCl}$, $E_{Ag/AgCl}^{\circ} = 0.197 \text{ V vs. SHE}$, pH=13.69. ^b Two electrode system. ^c $R = \mu\text{mol h}^{-1} \text{ cm}^{-2}$. ^d S is given in percentage. ^e R_{HF} is in $\mu\text{mol h}^{-1}$.

These results suggested that both FA and HF followed the ECH mechanism for the conditions reported in our study using Cu-NPNI/NF.

The change in the cumulative concentration of FF, FA and HF with respect to time was also analyzed for (i) a blank run (B) which accounts for all non-electrochemical reactions such as the Cannizzaro reaction,³¹ FF adsorption on the membrane surface, and transport of FF towards the anolyte, and (ii) electrochemical reaction in conjunction with the reactions occurring in the blank sample (E + B) (Fig. 3d). In the blank sample (B), the concentration of FF decreased and the concentration of FA increased with time, primarily due to the Cannizzaro reaction of FF in the presence of a base.³² The decrease in the FF concentration with time was also partly due to FF absorption into Nafion® (Fig. S8†) and the continuous transport of FF concentration to the anode compartment (Fig. S9†). The FA and HF concentrations remained constant throughout the electrolysis duration upon reaching a certain concentration, confirming that no ECH had occurred (Fig. 3d). The carbon balance for sample B after 1 h of mixing of FF and NaOH showed 92% of carbon recovery, confirming some FF loss *via* absorption and other means. Similarly, for the E + B sample, an 85% carbon recovery was obtained after the application of a working electrode potential of -1.45 V for 1 h (Fig. 3d). The difference in the carbon recovery between the B and E + B samples was attributed to the evaporation of high vapor pressure products (*e.g.* methyl furan), polymer formation, and irreversible adsorption of FF on surfaces.^{16,50}

The FF ECH at Cu-NPNI/NF was performed for five consecutive runs for the electrolysis duration of 1 h for each run at the applied potential of -1.45 V (Fig. S12a and b†). Before and

after FF ECH, the XRD analysis revealed similar XRD features indicating no change in the bulk crystal framework during the reaction. A slight positive shift in the XRD features of Cu suggested Cu lattice contraction (0.2%) due to an increase in the Cu-Ni interaction in the presence of a negative potential (Fig. S12c†). SEM analysis depicted no change in the morphology of Cu-NPNI/NF (Fig. S12d†). The XPS analysis represented a change in the surface-electronic states due to the transfer of electrons for FF ECH (Fig. 4 and 5). A small decrease in R_{FA} , R_{HF} and % conversion of FF was due to a small change in lattice parameters and surface-electronic states. The overall analysis of R_{FA} , R_{HF} , XRD, SEM and XPS indicated the suitability of the catalyst for long-term FF ECH operation.

3.3 Correlation of % selectivity and rate of formation for various electrodes

The % *S* and *R* for FA and HF were entirely dependent upon the ability of the electrode surface to generate H_{ads} and FF_{ads} . This ability was quite different for NF, NPNI/NF and Cu-NPNI/NF electrodes due to differences in their surface-chemical and electronic states. XPS studies were performed for NF, NPNI/NF and Cu-NPNI/NF to understand the electronic and chemical state of the various elements in these electrodes before and after the ECH of FF. The Ni-2p spectrum of NF (Fig. 4a) mainly exhibited a doublet of two peaks 2p_{3/2} (853 eV) and 2p_{1/2} (~873 eV), each resulting from the spin orbit coupling which typically represented NiO.^{56,57} Further peak splitting of the 2p_{3/2} peak into two peaks at 853 and ~855 eV, respectively, occurred due to screening of the electron resulting from hybridisation of the Ni-3d orbital with the O-2p valence orbital in the NiO lattice.⁵⁸

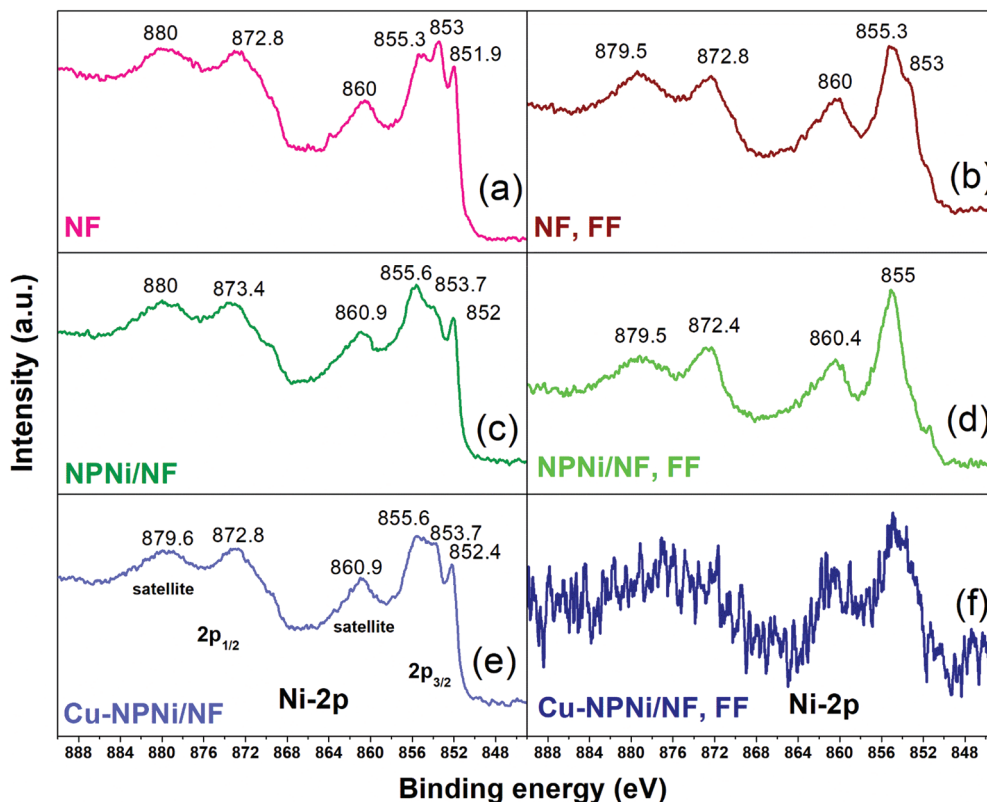


Fig. 4 XPS spectra of Ni-2p for (a) NF, (b) NF after FF ECH (NF and FF), (c) NPNi/NF, (d) NPNi/NF after FF ECH (NPNi/NF and FF), (e) Cu-NPNi/NF, (f) Cu-NPNi/NF after FF ECH (Cu-NPNi/NF and FF). FF ECH operating conditions: -1.45 V, 1 h, 50 mM FF + 0.5 M NaOH.

There was another peak at 851.9 eV that was attributed to the Ni component in the Ni^0 state.⁵⁸ Therefore, the XPS Ni-2p analysis of the NF confirmed the formation of NiO along with Ni metal (Fig. 4a). NiO is an insulator by nature, however, the presence of non-stoichiometry and hydroxides on the surface of NiO makes it conductive.^{59,60} The presence of NiO on the NF surface limited its ability to form H_{ads} and subsequently checked the formation of FA, whereas available FF_{ads} combined with another FF_{ads} in the presence of applied potential and formed HF. For this reason, there was no FA detected on NF, while the R_{HF} and % S_{HF} were $49.1 \pm 4.9 \mu\text{mol h}^{-1} \text{cm}^{-2}$ and $35.5 \pm 1.8\%$ respectively at -1.45 V after 1 h of ECH. In samples taken after FF ECH (Fig. 4b), the Ni- $2p_{3/2}$ spectrum at 855.3 eV binding energy for NF had relatively more intensity when compared to that of the peak at 853 eV, suggesting the presence of Ni-OH as well as Ni-O on the surface.⁵⁸ The peak corresponding to Ni^0 (851.9 eV) disappeared (Fig. 4b) because the Ni metal formed during the reduction process was subsequently solvated in the electrolyte medium to form surface $\text{Ni}(\text{OH})_2$. The Ni- $2p_{3/2}$ spectrum for NPNi/NF before FF ECH (Fig. 4c) suggested the formation of $\text{Ni}(\text{OH})_2$ along with non-stoichiometry in NiO.⁵⁸ The passivation of Ni on NPNi/NF was confirmed *via* the formation of $\text{Ni}(\text{OH})_2$ and this phenomenon was also reported elsewhere.^{61,62} $\text{Ni}(\text{OH})_2$ formation rendered the surface of the NPNi/NF to be very conductive and enhanced H_{ads} formation.^{63,64} Therefore the R_{FA} as well as %

S_{FA} ($14.4 \pm 2.7 \mu\text{mol h}^{-1} \text{cm}^{-2}$, $9.0 \pm 0.6\%$) were enhanced and R_{HF} as well as % S_{HF} ($15.7 \pm 6.7 \mu\text{mol h}^{-1} \text{cm}^{-2}$, $19.4 \pm 1\%$) were decreased when compared to NF at -1.45 V applied potential and 1 h of ECH. The Ni- $2p_{3/2}$ spectrum of the NPNi/NF catalyst after the FF ECH (Fig. 4d) showed the complete disappearance of the peak at 853 eV as well as the presence of the peak at 855 eV. This suggested the hydroxylation of the Ni by the solvation of the Ni formed by complete reduction of the surface phase during FF ECH. The Ni- $2p_{3/2}$ spectrum for Cu-NPNi/NF before FF ECH (Fig. 4e) was analysed and it was concluded that the ratio of the intensities of signature peaks of Ni-O at 855.6 eV and 853.7 eV for Cu-NPNi/NF was almost 1 : 1 which suggested strong non stoichiometry in the NiO generated during Cu deposition on NPNi/NF (Fig. 4e).⁵⁸ The peak corresponding to Ni^0 was obtained at 852.4 eV in Cu-NPNi/NF, a 0.5 eV higher binding energy as compared Ni^0 in NF, confirming an electronic interaction between the Ni^0 and the deposited Cu.⁶⁵ The Ni-2p spectrum peaks for Cu-NPNi/NF after FF ECH were not clearly visualized (Fig. 4f) because the presence of Cu enhanced FF adsorption, blocking the surface of the electrode. This confirmed that the presence of FF_{ads} was the reason for enhanced R_{FA} , R_{HF} , % S_{FA} , and % S_{HF} on Cu-NPNi/NF electrodes.

The XPS O-1s spectrum (Fig. 5) comprised peaks at 528.9 eV, 531 eV, and 533.4 eV corresponding to the $-\text{O}$ of the NiO lattice, surface $-\text{OH}$ group, and surface H_2O , respectively.^{56,57}

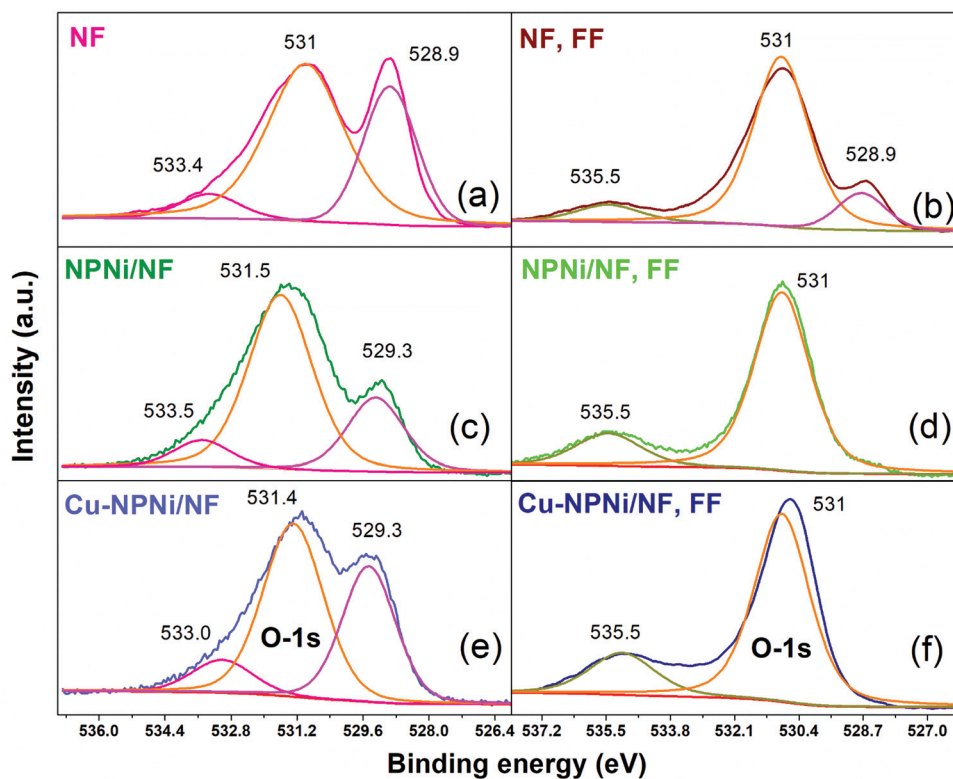


Fig. 5 XPS spectra of O-1s for (a) NF, (b) NF after FF ECH (NF and FF), (c) NPNI/NF, (d) NPNI/NF after FF ECH (NPNI/NF and FF), (e) Cu-NPNI/NF, (f) Cu-NPNI/NF after FF ECH (Cu-NPNI/NF and FF). FF ECH operating conditions: -1.45 V, 1 h, 50 mM FF + 0.5 M NaOH.

The ratio of the ~ 531.4 peak area for NF, NPNI/NF and Cu-NPNI/NF (Fig. 5a, c and e) was 1 : 1.2 : 0.85, confirming that Ni-OH was formed during NPNI/NF electrode preparation and that a fraction of this Ni-OH was subsequently reduced during Cu deposition to fabricate Cu-NPNI/NF electrodes; these results corroborated with the Ni-2p XPS data. The ratio of area under the ~ 529 eV peak for NF and NPNI/NF (Fig. 5a and c) was 1 : 0.77 confirming less presence of the NiO on the NPNI/NF surface due to the reduction of NiO during electrode preparation. Post FF ECH, the lattice O representing the NiO was still present only for the NF electrocatalyst (Fig. 5b, d and f) which was likely due to the excessive availability of NiO on NF that did not reduce completely. The disappearance of the peak at ~ 533 eV and the appearance of a peak at 535.5 eV were attributed to the coverage of the electrode surface by FF and other organics (FA and HF). The ratio of area under this peak (535.5 eV) for NF, NPNI/NF and Cu-NPNI/NF was 1 : 1.75 : 2.28, confirming the highest adsorbed oxygen (due to organics) in Cu-NPNI/NF and further validating the observations shown in Fig. 4f. The Cu-2p_{3/2} XPS spectra (Fig. S10†) for Cu-NPNI/NF and Cu plate before FF ECH were compared and it was observed that the Cu⁰ peak (931.8 eV) on Cu-NPNI/NF shifted towards a higher binding energy of 1.3 eV as compared to the Cu⁰ peak on Cu plate (930.5 eV). This increase in binding energy was attributed to the electronic interaction between Cu and NPNI/NF along with Cu phase segregation, which signified the formation of bimetallic Ni-Cu.⁶⁵ The XPS analysis con-

firmed the presence of NiO on the NF surface and the presence of Ni(OH)₂ on NPNI/NF. Ni(OH)₂ is reported to have better H_{ads} affinity as compared to NiO. The poor H_{ads} property of NF resulted in a 1.3-fold higher R_{HF} and no R_{FA} as compared to NPNI/NF at -1.45 V after 1 h of ECH. The surface analysis of NF and NPNI/NF through XPS determined the H_{ads} affinity and supported the conclusion that FA and HF production was dependent on H_{ads} affinity, similar to the conclusion in an earlier section for benchmark catalysts (Cu, Pt, and NF). The XPS for Cu-NPNI/NF confirmed that the electronic interaction of Cu and Ni enhanced FF_{ads} and consequently the rate of formation of FA and HF on Cu-NPNI/NF.

4. Conclusion

Electrocatalytic hydrogenation of furfural, a model bio-oil compound, was performed with NF, Cu, Pt, NPNI/NF and Cu-NPNI/NF electrocatalysts in an alkaline electrolyte. Cu was identified to be the best catalyst for the generation of furfuryl alcohol and hydrofuroin while NF was unable to produce furfuryl alcohol. The percentages of S_{FA} and R_{FA} depended upon the catalyst's property to generate H_{ads} . Hydrofuroin formation was observed at high potentials on Pt where H_{ads} was preferred over the HER. Hydrofuroin formation was also observed on NF where H_{ads} was not generated effectively. Hence, the absence of H_{ads} and excess H_{ads} resulted in hydrofuroin formation.

Porous Ni was generated on NF by electrochemical co-deposition of Ni–Cu followed by selective etching of Cu. NPNi/NF showed the highest HER current among other prepared porous electrodes, which showed that it favored high H_{ads} . NPNi/NF generated higher amounts of furfuryl alcohol and lesser hydrofuroin because of its intermediate H_{ads} property as compared to NF and Pt. Furthermore, Cu was deposited on the NPNi/NF substrate (designated as Cu–NPNi/NF) to get Cu nanoplates and the resultant bimetallic Ni–Cu generated higher amounts of furfuryl alcohol and hydrofuroin as compared to Cu, NF and NPNi/NF. The production of furfuryl alcohol and hydrofuroin and % conversion of FF on Cu–NPNi/NF were determined by varying the electrode potential and electrolysis duration. XPS studies showed that the presence of NiO on NF, Ni(OH)₂ on NPNi/NF, and bimetallic Ni–Cu along with non-stoichiometry of NiO on Cu–NPNi/NF played a significant role in the electrocatalyst's affinity for furfural electrocatalytic hydrogenation. Cu–NPNi/NF produced the highest R_{FA} and R_{HF} , 118.7 ± 8 and $176.3 \pm 3.4 \mu\text{mol h}^{-1} \text{cm}^{-2}$ at $-1.45 \text{ V vs. Ag/AgCl/sat KCl}$ after 1 h of electrolysis as per the analysis of the relevant alkaline electrolyte compound that is available in the literature. This study also provides comprehensive information about the formation of hydrofuroin as a function of operating parameters such as applied potential and duration of electrocatalytic hydrogenation.

Conflicts of interest

There are no conflicts of interest to declare.

Acknowledgements

The authors acknowledge Indian Institute of Technology, Delhi; Bioenergy-Awards for Cutting Edge Research (B-ACER) Fellowship sponsored by Department of Biotechnology and Indo-US Science and Technology Forum, India; and Washington University in St Louis, USA for the financial support at various stages. The authors want to thank Nano Research Facility, IIT Delhi as well as WUSTL for the use of HPLC and GC-MS instruments. The authors would like to appreciate the help from the Institute of Materials Science and Engineering (IMSE), WUSTL for the use of FE-SEM and XPS. VR would like to thank the VAJRA adjunct faculty scheme sponsored by the Department of Science and Technology, India.

References

- 1 A. Satlewal, R. Agrawal, S. Bhagia, P. Das and A. J. Ragauskas, *Biofuels, Bioprod. Biorefin.*, 2018, **12**, 83–107.
- 2 How stubble burning in Haryana & Punjab is the biggest culprit for poor air quality in Delhi, <https://economictimes.indiatimes.com/news/politics-and-nation/how-stubble-burning-is-the-biggest-culprit-for-poor-air-quality-in-delhi-a-ground-report-from-haryana-punjab/articleshow/61609110.cms>, (accessed 16 October 2018).
- 3 NREL, https://www.nrel.gov/continuum/sustainable_transportation/cellulosic_ethanol.html, (accessed 28 October 2018).
- 4 V. S. Sikarwar, M. Zhao, P. S. Fennell, N. Shah and E. J. Anthony, *Prog. Energy Combust. Sci.*, 2017, **61**, 189–248.
- 5 M. B. Griffin, K. Iisa, H. Wang, A. Dutta, K. A. Orton, R. J. French, D. M. Santosa, N. Wilson, E. Christensen, C. Nash, K. M. Van Allsburg, F. G. Baddour, D. A. Ruddy, E. C. D. Tan, H. Cai, C. Mukarakate and J. A. Schaidle, *Energy Environ. Sci.*, 2018, **11**, 2904–2918.
- 6 G. Afreen, S. Pathak and S. Upadhyayula, *Chem. Eng. J.*, 2020, **400**, 125824.
- 7 Y. Wang, Z. Zeng, X. Tian, L. Dai, L. Jiang, S. Zhang, Q. Wu, P. Wena, G. Fua, Y. Liua and R. Ruana, *Bioresour. Technol.*, 2018, **269**, 162–168.
- 8 Y. Yang, Y. Zhang, E. Omairey, J. Cai, F. Gu and A. V. Bridgwater, *J. Cleaner Prod.*, 2018, **187**, 390–399.
- 9 R. O. Arazo, D. A. D. Genuino, M. D. G. de Luna and S. C. Capareda, *Sustainable Environ. Res.*, 2017, **27**, 7–14.
- 10 X. Liu, B. Li, G. Han, X. Liu, Z. Cao, D. en Jiang and Y. Sun, *Nat. Commun.*, 2021, **12**, 1–11.
- 11 C. Zhao and J. A. Lercher, *Angew. Chem.*, 2012, **124**, 6037–6042.
- 12 X. Wang and R. Rinaldi, *Angew. Chem., Int. Ed.*, 2013, **52**, 11499–11503.
- 13 M. W. Nolte, A. Saraeian and B. H. Shanks, *Green Chem.*, 2017, **19**, 3654–3664.
- 14 A. S. May and E. J. Biddinger, *ACS Catal.*, 2020, **10**, 3212–3221.
- 15 R. Chauhan and V. C. Srivastava, *Process Saf. Environ. Prot.*, 2021, **147**, 245–258.
- 16 R. Trane-Restrup and A. D. Jensen, *Appl. Catal., B*, 2015, **165**, 117–127.
- 17 R. Mariscal, P. Maireles-Torres, M. Ojeda, I. Sádaba and M. López Granados, *Energy Environ. Sci.*, 2016, **9**, 1144–1189.
- 18 K. Okano, *Tetrahedron*, 2011, **67**, 2483–2512.
- 19 X. Shang, Y. Yang and Y. Sun, *Green Chem.*, 2020, **22**, 5395–5401.
- 20 W. C. Albert and A. Lowy, *Trans. Electrochem. Soc.*, 1939, **75**, 367–375.
- 21 P. Nilges and U. Schröder, *Energy Environ. Sci.*, 2013, **6**, 2925–2931.
- 22 L. Liu, H. Liu, W. Huang, Y. He, W. Zhang, C. Wang and H. Lin, *J. Electroanal. Chem.*, 2017, **804**, 248–253.
- 23 X. H. Chadderdon, D. J. Chadderdon, J. E. Matthesen, Y. Qiu, J. M. Carraher, J. P. Tessonnier and W. Li, *J. Am. Chem. Soc.*, 2017, **139**, 14120–14128.
- 24 B. Zhao, M. Chen, Q. Guo and Y. Fu, *Electrochim. Acta*, 2014, **135**, 139–146.
- 25 F. Wang, M. Xu, L. Wei, Y. Wei, Y. Hu, W. Fang and C. G. Zhu, *Electrochim. Acta*, 2015, **153**, 170–174.
- 26 S. Jung and E. J. Biddinger, *ACS Sustainable Chem. Eng.*, 2016, **4**, 6500–6508.

- 27 Y. Zhu, W. Li, Y. Lu, T. Zhang, H. Jameel, H. M. Chang and L. Ma, *RSC Adv.*, 2017, **7**, 29916–29924.
- 28 L. K. E. Park, S. Ren, S. Yiacoumi, X. P. Ye, A. P. Borole and C. Tsouris, *Energy Fuels*, 2016, **30**, 2164–2173.
- 29 N. Mahmood, Y. Yao, J. W. Zhang, L. Pan, X. Zhang and J. J. Zou, *Adv. Sci.*, 2018, **5**, 1700464.
- 30 B. S. De, A. Singh, A. Elias, N. Khare and S. Basu, *Sustainable Energy Fuels*, 2020, **4**, 6234–6244.
- 31 O. Kikhtyanin, E. Lesnik and D. Kubička, *Appl. Catal., A*, 2016, **525**, 215–225.
- 32 P. Parpot, A. P. Bettencourt, G. Chamoulaud, K. B. Kokoh and E. M. Belgsir, *Electrochim. Acta*, 2004, **49**, 397–403.
- 33 C. H. Lam, C. B. Lowe, Z. Li, K. N. Longe, J. T. Rayburn, M. A. Caldwell, C. E. Houdek, J. B. Maguire, C. M. Saffron, D. J. Miller and J. E. Jackson, *Green Chem.*, 2015, **17**, 601–609.
- 34 B. S. Takale, X. Feng, Y. Lu, M. Bao, T. Jin, T. Minato and Y. Yamamoto, *J. Am. Chem. Soc.*, 2016, **138**, 10356–10364.
- 35 M. Goepel, H. Kabir, C. Küster, E. Saraçi, P. Zeigermann, R. Valiullin, C. Chmelik, D. Enke, J. Kärger and R. Gläser, *Catal. Sci. Technol.*, 2015, **5**, 3137–3146.
- 36 B. You, N. Jiang, M. Sheng, M. W. Bhushan and Y. Sun, *ACS Catal.*, 2016, **6**, 714–721.
- 37 J.-K. Chang, S.-H. Hsu, I.-W. Sun and W.-T. Tsai, *J. Phys. Chem. C*, 2008, **112**, 1371–1376.
- 38 M. A. Lukowski, A. S. Daniel, F. Meng, A. Forticaux, L. Li and S. Jin, *J. Am. Chem. Soc.*, 2013, **135**, 10274–10277.
- 39 Y. Wei, H. Lei, L. Wang, L. Zhu, X. Zhang, Y. Liu, S. Chen and B. Ahring, *Energy Fuels*, 2014, **28**, 1207–1212.
- 40 B. Chatterjee and C. Gunanathan, *Org. Lett.*, 2015, **17**, 4794–4797.
- 41 K. Chen, J.-L. Ling and C.-D. Wu, *Angew. Chem., Int. Ed.*, 2019, **58**, 2–9.
- 42 Z. Jamil, E. Ruiz-Trejo and N. P. Brandon, *J. Electrochem. Soc.*, 2017, **164**, D210–D217.
- 43 M. Fleischmann and A. Saraby-Reintjes, *Electrochim. Acta*, 1983, **29**, 69–75.
- 44 B. Seemala, C. M. Cai, C. E. Wyman and P. Christopher, *ACS Catal.*, 2017, **7**, 4070–4082.
- 45 K. K. Patra, P. A. Bharad, V. Jain and C. S. Gopinath, *J. Mater. Chem. A*, 2019, **7**, 3179–3189.
- 46 J. M. Lee, K. K. Jung and J. S. Ko, *J. Electrochem. Soc.*, 2016, **163**, D407–D413.
- 47 B. Liu, L. Cheng, L. Curtiss and J. Greeley, *Surf. Sci.*, 2014, **622**, 51–59.
- 48 N. Shan, M. K. Hanchett and B. Liu, *J. Phys. Chem. C*, 2017, **121**, 25768–25777.
- 49 S. Sitthisa, T. Sooknoi, Y. Ma, P. B. Balbuena and D. E. Resasco, *J. Catal.*, 2011, **277**, 1–13.
- 50 X. Yang, A.-Y. Lu, Y. Zhu, M. N. Hedhili, S. Min, K.-W. Huang, Y. Han and L.-J. Li, *Nano Energy*, 2015, **15**, 634–641.
- 51 S. Jung, A. N. Karaiskakis and E. J. Biddinger, *Catal. Today*, 2019, **323**, 26–34.
- 52 M. Y. Gao, C. Yang, Q. B. Zhang, Y. W. Yu, Y. X. Hua, Y. Li and P. Dong, *Electrochim. Acta*, 2016, **215**, 609–616.
- 53 S. Ghosh, S. Hariharan and A. K. Tiwari, *J. Phys. Chem. C*, 2017, **121**, 16351–16365.
- 54 J. J. Roylance, T. W. Kim and K. S. Choi, *ACS Catal.*, 2016, **6**, 1840–1847.
- 55 X. H. Chadderton, D. J. Chadderton, T. Pfennig, B. H. Shanks and W. Li, *Green Chem.*, 2019, **21**, 6210–6219.
- 56 M. A. Peck and M. A. Langell, *Chem. Mater.*, 2012, **24**, 4483–4490.
- 57 I. Preda, R. J. O. Mossaneck, M. Abbate, L. Alvarez, J. Méndez, A. Gutiérrez and L. Soriano, *Surf. Sci.*, 2012, **606**, 1426–1430.
- 58 A. P. Grosvenor, M. C. Biesinger, R. S. C. Smart and N. S. McIntyre, *Surf. Sci.*, 2006, **600**, 1771–1779.
- 59 F. J. Morin, *Phys. Rev.*, 1954, **93**, 1199–1204.
- 60 R. W. Wright and J. P. Andrews, *Proc. Phys. Soc., London, Sect. A*, 1949, **62**, 446–455.
- 61 D. S. Hall, C. Bock and B. R. Macdougall, *J. Electrochem. Soc.*, 2013, **160**, 235–243.
- 62 J. R. Vilche and A. J. Arvia, *Corros. Sci.*, 1978, **18**, 441–463.
- 63 J. Wei, M. Zhou, A. Long, Y. Xue, H. Liao, C. Wei and Z. J. Xu, *Nano-Micro Lett.*, 2018, **10**, 1–15.
- 64 X. Yu, J. Zhao, L. Zheng, Y. Tong, M. Zhang, G. Xu, C. Li, J. Ma and G. Shi, *ACS Energy Lett.*, 2017, **3**, 237–244.
- 65 A. R. Naghash, T. H. Etsell and S. Xu, *Chem. Mater.*, 2006, **18**, 2480–2488.
- 66 X. Zhang, M. Han, G. Liu, G. Wang, Y. Zhang, H. Zhang and H. Zhao, *Appl. Catal., B*, 2019, **244**, 899–908.